Journal of Constructional Steel Research 182 (2021) 106650

Contents lists available at ScienceDirect

Journal of Constructional Steel Research

journal homepage: www.elsevier.com/locate/jcsr

Flexural tests of concrete-encased composite girders with high-strength steel angle

Jong-Jin Lim [a], Jin-Yong Kim [a], Jin-Won Kim [b], Tae-Sung Eom [c,*]

[a] Senvex, Beodeunaru-ro 19-gil, Yeongdeungpo-gu, Seoul 07226, Republic of Korea
[b] POSCO Global R&D Center, 100 Sondokwahak-ro, Yeonsu-gu, Incheon, Republic of Korea
[c] Dept. of Architectural Engineering, Dankook Univ., 152 Jukjeon-ro, Gyeonggi-do, 448-701, Republic of Korea

ARTICLE INFO

Article history:
Received 7 December 2020
Received in revised form 7 March 2021
Accepted 9 March 2021
Available online xxxx

Keywords:
Steel angle
High-strength steel
Composite beam
Strain compatibility analysis
Composite structure

ABSTRACT

This study investigated the flexural behavior of concrete-encased steel angle girders (PSRC girders). Inside the concrete section, high-strength steel angles (F_y = 605 MPa) with unequal legs were used as longitudinal reinforcement, and diagonal and vertical members were bolt-connected to the longitudinal angles as transverse ties. Flexural tests were performed for three PSRC girder specimens with different reinforcement details. The tests showed that the PSRC girders all developed the peak loads exceeding the nominal strengths; however, the ductility was limited as rupture occurred near bolt holes in the longitudinal angles. Overall, the concrete damage and cracking of the PSRC girders were comparable to those in conventional reinforced concrete beams, and cover spalling and bond deterioration along the longitudinal angles were not severe. The strength, stiffness, and ductility estimated in accordance with current design codes were compared with the test results. Given the investigation results, the application and design considerations of PSRC girders were discussed.

1. Introduction

Fig. 1 shows the concrete-encased steel angle girder (prefabricated steel-reinforced concrete girder or PSRC girder) using steel angles as longitudinal and transverse reinforcements [5,6]. Compared to conventional concrete-encased steel beams, the PSRC girder may be more efficient in resisting bending because high-strength steel angles are placed along the perimeter of the concrete section. Besides, by making up a Pratt or Warren truss with longitudinal, diagonal, and vertical angles, the PSRC girder can resist working loads without temporary props during construction. By using steel forms (thickness 1.6– 2.3 mm) engaging with vertical angles, on-site concrete formwork may be minimized (see Fig. 1).

The applicability of PSRC members (i.e., concrete-encased steel angle members) to columns has been experimentally and analytically investigated by many Korean researchers [4–13]. For example, Kim et al. [10] performed the eccentric compressive tests of PSRC columns with high-strength steel angles (F_y = 806 MPa – 914 MPa) and high-strength concrete (f_c' = 94 MPa – 184 MPa). The results showed that the flexural strength and flexural stiffness of the PSRC columns were greater than those of the conventional concrete-encased H-section columns. In addition, the composite action between the high-strength steel and concrete was accurately predicted by a strain-compatibility analysis. Kim et al. [12,13] investigated the compressive behavior of concentrically and eccentrically loaded PSRC columns. Longitudinal steel angles and transverse ties (i.e. flat bars or *Z*-shaped bars) were connected by bolting, without welding. The results showed that reduction in the cross section of steel angles due to hole drilling significantly affected the strengths of the PSRC columns. Eom et al. [6] investigated the compressive behavior of PSRC columns with high-strength cold-formed steel angles. The stress-strain behavior of the cold-formed angle changed locally near the bent corner due to the strain-hardening behavior and residual plastic strains. However, the overall behavior of the PSRC columns was reasonably estimated based on the stress-strain behavior before cold-forming. Even under pure compression, the strength and stiffness were deteriorated by reduction in the cross-sectional area due to hole drilling, as reported in the literature [12,13].

Unlike the previous studies that mostly dealt with the axial compressive behavior of concentrically or eccentrically loaded PSRC columns, Eom et al. [4] investigated the flexural strength, ductility, and failure mode of PSRC columns. The tests showed that as crushing and spalling occurred early at the concrete cover, bond deterioration developed along the top and bottom longitudinal angles. Ultimately, rupture occurred not only at the longitudinal angles, but also the transverse bars welded on the angle surface.

The PSRC girder in Fig. 1 that is developed to use as large-scale girders in warehouse buildings, is different from the previous one, as follows. First, high-strength steel angles fabricated by cold-forming

* Corresponding author.
E-mail addresses: Jwkim10@posco.com (J.-W. Kim), tseom@dankook.ac.kr (T.-S. Eom).

https://doi.org/10.1016/j.jcsr.2021.106650
0143-974X/

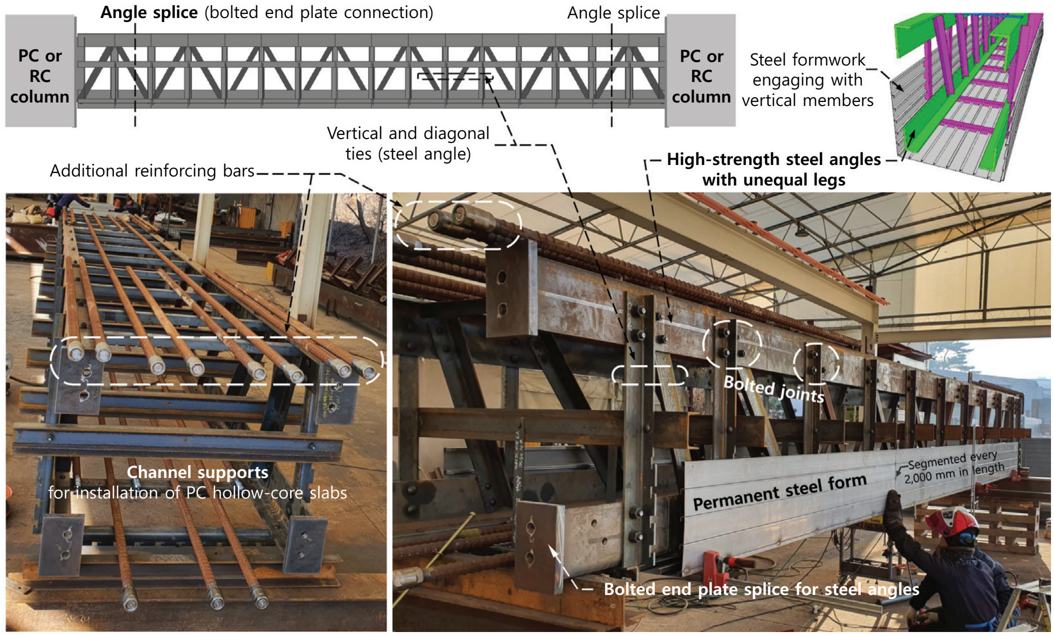

Fig. 1. Concrete-encased steel angle composite girder system (or PSRC girder system).

(that is, press bending at room temperature), instead of hot-rolling, are used as tensile reinforcement for gravity loads. Since cold-formed steel angles may have different properties locally near the bent corner, care should be taken. Second, since transverse ties are bolt-connected to the longitudinal angles, reduction in the cross section due to hole-drilling may affect the strength and ductility of the PSRC member. Particularly, such area loss can reach up to 20% of the gross area. Third, steel forms are used as permanent steel sheathing. Although the steel forms barely contribute to the flexural and shear strength at ultimate limit state, it may reduce concrete cracking under service loading. Thus, the effects of the steel forms on the flexural behavior need to be investigated.

In this study, flexural tests of three large-scale PSRC girders with different reinforcement details were performed. The load-deflection relationships and failure mode of the PSRC girders were investigated, and the effects of test parameters on the structural performance such as strength and ductility were discussed. The nominal values of flexural stiffness, strength, and ductility predicted in accordance with provisions of current design codes were compared with the test values. Based on the results, the applicability and design considerations of PSRC girders were discussed.

2. Test program

2.1. Specimen details

Fig. 2 shows the configuration and reinforcement details of three PSRC girder specimens, PB1, PB2, and PB3. The dimensions of the concrete section were $b = 820$ mm (width) and $h = 1060$ mm (depth) in all specimens. The whole length of the girder was 10,100 mm and the shear span between the loading point and the nearer support was $l_s =$ 3500 mm. Although the span of prototype girders was larger than 15,000 mm, the girder length and shear span ratio was adjusted to 10,100 mm and $l_s/h = 3.3$ for flexural tests in the laboratory.

For the control specimen PB1, cold-formed high-strength steel angles with unequal legs, L-200 × 105 × 15, were used as flexural reinforcement at the four corners of the concrete section. The overall widths of unequal legs were 200 mm and 105 mm, and the thickness was 15 mm. For transverse ties, hot-rolled steel angles, L-65 × 65 × 6 (vertical) and L-90 × 90 × 9 (diagonal), were used. The vertical and diagonal ties were bolt-connected to the longitudinal angles. Each bolted joint used two high-tension bolts, 2-F10T M16 bolts. The specified design tensile strength and diameter of F10T M16 bolts were $F_u = 1000$ MPa and d_b $= 16$ mm, respectively. The two longitudinal angles at the top or bottom were bolt-connected by horizontal ties (L-65 × 65 × 6) placed in the width direction of the girder; each bolted joint had one F10T M16 bolt. As shown in the cross section PB1 in Fig. 2, the thickness of the cover concrete measuring from the outer surface of longitudinal angles was 75 mm, larger than 50 mm used in the previous tests [4]. Such thick cover concrete was used to alleviate premature spalling and crushing of the cover concrete. Furthermore, in order that parts of bond forces were transferred directly to the core concrete, the diagonal angles were connected to the inner surface of longitudinal angles by bolting.

PB2 used the same prefabricated details of longitudinal and transverse angles as those of PB1, except steel forms (thickness 1.6 mm) were used as permanent sheathing (see the cross section PB2 in Fig. 2 and the photo PB2 in Fig. 3). The height of steel forms was 620 mm from the bottom and segmented every 2000 mm in length for easier installation (see Fig. 1). On the inner surface of steel forms, six L-shaped ribs engaged with the vertical ties (angles) by clipping on and were embedded within the cover concrete (thickness 75 mm). Given that steel forms were segmented every 2000 mm in length, it was expected that the contribution of steel forms to flexural strength would be limited. However, the segmented steel forms engaging with the vertical ties were expected to reduce concrete cracking and spalling. Note that, given that precast concrete hollow core slabs are placed on top of channel supports in actual construction site (see Fig. 1), partial-depth steel forms (i.e., height 620 mm) were used in PB2.

PB3 used the same prefabricated details of longitudinal and transverse angles as those of PB1, except five D32 reinforcing bars (diameter 31.8 mm) were additionally used at the bottom (see the cross section PB3 in Fig. 2 and the photo PB3 in Fig. 3). PB3 was planned to investigate composite action between the high-strength angles and reinforcing bars.

2.2. Material properties

The objective of this study was to investigate the behavior of PSRC girders with high-strength steel angles of design yield strength 460 MPa or greater. However, such high-strength angles were not available in

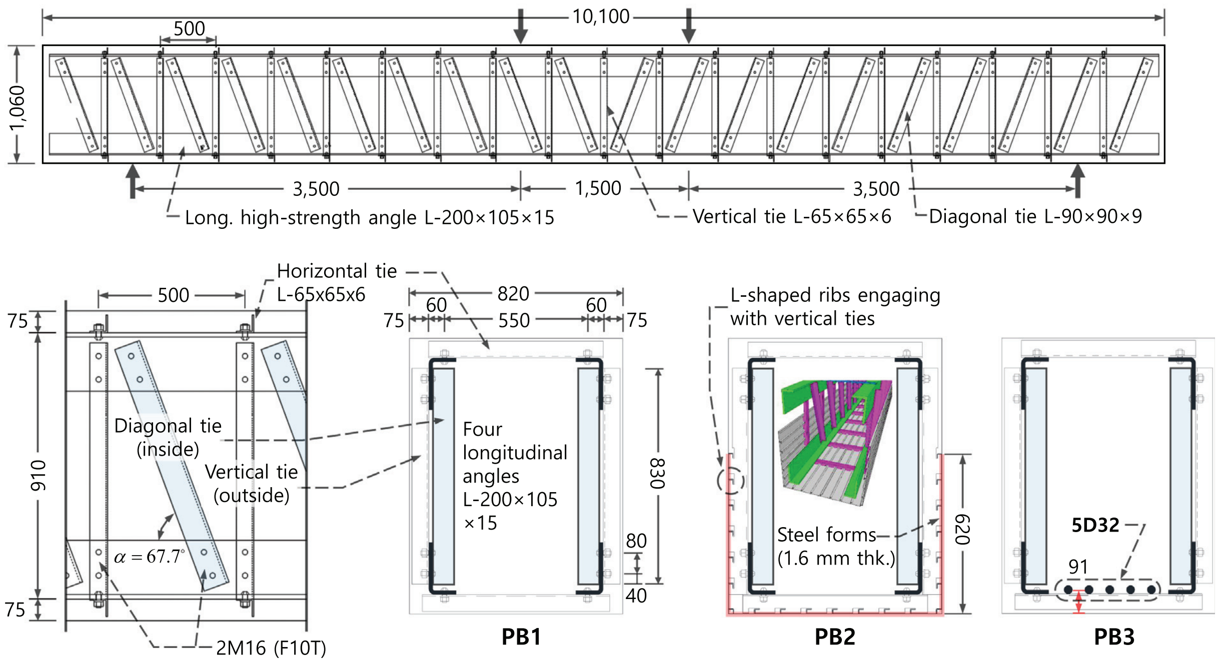

Fig. 2. Details of PSRC girder specimens (mm).

hot-rolled products. Thus, the high-strength angles were fabricated by cold-forming (that is, press bending at room temperature). Fig. 4 (a) shows the cold-formed high-strength steel angle L-200 × 105 × 15 used as the flexural reinforcement in the PSRC girders. Since the angle was fabricated by bending a long, narrow, planar plate with width 283 mm and thickness 15 mm using the press machine (edge radius R = 9 mm), the section geometry was different from that of hot-rolled sections [6]. The cross-sectional area of the angle was $A_a = 283 \cdot 15 = 4240$ mm^2. Fig. 4 (b) shows the strains measured on the surface of the angle in the width direction during press bending. The bent corner of the angle (CH1 and CH2) underwent tensile strains due to convex bending. The strain rate during the bending was approximately 0.00245 [mm/mm]/s for CH1 and 0.00234 [mm/mm]/s. Note that, CH1 and CH2 were malfunctioned at 16 s and 18 s, respectively, as output voltages of the strain gauges overflowed the setting range of the data logger.

Table 1 shows the yield strength, ultimate strength, and the elongation strain at rupture of the steel used for the PSRC girder specimens. Fig. 5 shows the stress-strain relationships of the angles and reinforcing bars. When measuring strains, rupture occurred at some distance away from the locations where the gauges were installed, or some gauges were malfunctioned early. Thus, the ultimate strength and rupture strain were measured using the testing machine data, rather than the stress-strain relationships in Fig. 5. For cold-formed high-strength steel angles (L-200 × 105 × 15) used as the flexural reinforcement, two tensile specimens were taken from the planar plate before press bending. The yield and ultimate strengths of cold-formed high-strength steel angle (L-200 × 105 × 15) were 605 and 672 MPa, respectively, and the stress continued to increase linearly until 0.06 mm/mm during the post-yield behavior (post-yield modulus E_p = 1070 MPa, see Fig. 5). According to Eom et al. [6], the yield and ultimate strengths at the bent corner of cold-formed high-strength steel angles were increased by 12% and 26%, respectively, over those at the free end, due to strain-hardening behavior. However, the strength changes of cold-formed angles occurred in a limited area near the bent corner. Consequently, the overall behavior of PSRC columns can be reasonably estimated based on the stress-strain behavior before cold-forming. Thus, this study investigated the flexural behavior of the PSRC girders based on the stress-strain behavior of the high-strength plate before press bending.

For hot-rolled steel angles (L-90 × 90 × 9 and L-65 × 65 × 6) used as vertical, diagonal, and horizontal ties, the specimens were taken from the free end of a leg. The yield and ultimate strengths (318 and 480 MPa for L-90 × 90 × 9 and 340 and 486 MPa for L-65 × 65 × 6) were less than those of the cold-formed high-strength angle. For D32 reinforcing bars used as the additional tensile reinforcement in PB3, the yield and ultimate strengths were 662 and 827 MPa,

Fig. 3. PSRC girder specimens under fabrication.

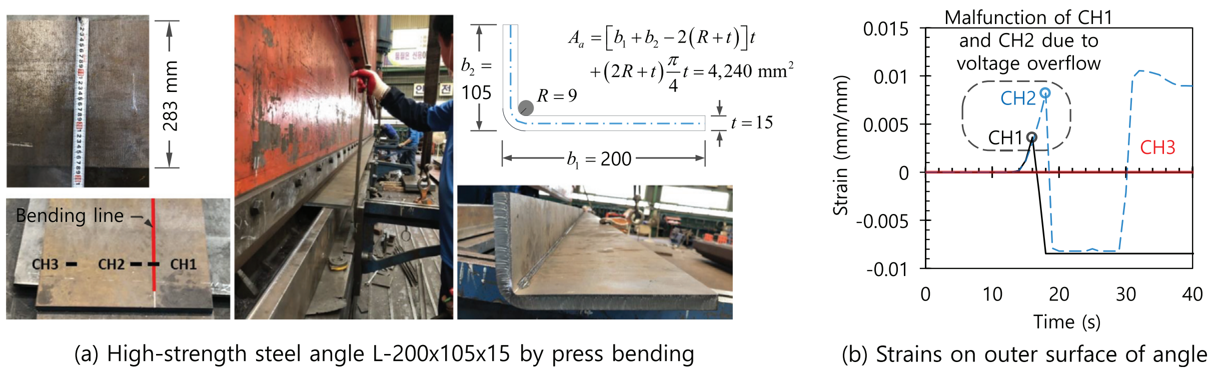

Fig. 4. High-strength steel angles fabricated by press bending.

Table 1
Material strengths.

Material		Yield strength	Ultimate strength	Elongation strain at rupture
Steel angles	L-200x105x15[1]	605 MPa	672 MPa	0.398
	L-90x90x9[1]	318 MPa	480 MPa	0.402
	L-65x65x6[1]	340 MPa	486 MPa	0.392
Steel forms	1.6 mm thick[1]	255 MPa	343 MPa	0.400
Reinforcing bar	D32[1]	662 MPa	827 MPa	0.360
Concrete	Cylinder (100 × 200)	Compressive strength = 36.3 MPa		

[1] The strength values were the mean of two specimens.

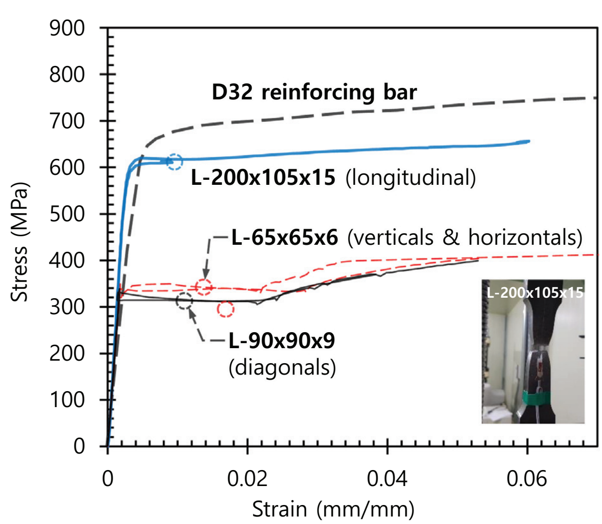

Fig. 5. Stress-strain relationships of steel angles and reinforcing bars.

respectively, and the post-yield behavior was almost linear (post-yield modulus $E_p = 1540$ MPa). The mean compressive strength of concrete cylinders at the testing day was 36.3 MPa.

2.3. Test setup

Fig. 6 shows the test setup of PSRC girder specimens. The universal testing machine (UTM) of a capacity 1000 kN was used for flexural testing. The UTM load was transferred at two loading points through a loading block on top of the specimen. The midspan region between the two loading points was 1500 mm long, and the shear span between the loading point and nearer support was $l_s = 3500$ mm long. The test was conducted at a speed of 0.003 mm/s in a displacement-control mode. The test was terminated when the load-carrying capacity of the specimen was approximately reduced to 50% of the maximum.

Deflections of the specimen were measured using 6 Linear Variable Displacement Transducers (LVDTs) installed at an interval of 750 mm in midspan (see Fig. 6). There was no LVDT or load cell used at the supports. To trace the strain development of steel members embedded within the concrete, 5 mm – strain gauges were glued on the surfaces of longitudinal, diagonal, and vertical angles.

3. Test results

3.1. Load–deformation relationships and failure modes

Fig. 7 shows the UTM load–deflection (P–δ) relationships in midspan of the PSRC girder specimens. Using the measured deflections δ_2, δ_3, and δ_4 in Fig. 7, the average curvature ϕ at the uniform bending region in midspan was calculated as follows. Assuming that the curvature at the midspan region is constant as ϕ and the deflected shape of the specimen is symmetrical (i.e., zero slope at the midspan) yields $[\delta_3 - \delta_2] = [\delta_3 - \delta_4] = 0.5\phi d_\delta^2$ (see Fig. 7 (d)). Thus,

$$\phi = \frac{1}{2}\left[\frac{2(\delta_3 - \delta_2)}{d_\delta^2} + \frac{2(\delta_3 - \delta_4)}{d_\delta^2}\right] = \frac{2\delta_3 - (\delta_2 + \delta_4)}{d_\delta^2} \tag{1}$$

where δ_2, δ_3, and δ_4 = vertical deflections measured at the left end, center, and right ends of the uniform bending region, respectively; d_δ = distance between the points where vertical deflections were measured (= 750 mm).

Fig. 8 shows the moment–curvature (M–ϕ) relationships in midspan of the PSRC girder specimens. Fig. 9 shows the variation of concrete cracks in midspan with increasing moment load. The moment load was computed as $M = 0.5Pl_s$, where P is the vertical load applied by the testing machine. In Fig. 8, the flexural stiffness $EI_{0.75}$ was calculated using the secant line connecting the origin and the pre-yield point of $0.75M_u$, where M_u = maximum moment load by test [4]. The yield point was then defined as the point where the secant line of the flexural stiffness $EI_{0.75}$ intersected with the horizontal line of M_u, and thus the yield curvature was calculated as $\phi_y = M_u / EI_{0.75}$. The failure point was defined as the post-peak point where the strength was deteriorated to $0.75M_u$, and then the curvature ductility was calculated as $\mu = \phi_u / \phi_y$, where ϕ_u = curvature at the failure point.

For the control specimen PB1 (see Figs. 8 (a) and 9 (a)), flexural yielding occurred at $\phi_y = 0.0074$ /m and the maximum load ($M_u = 3560$ kN-m) reached at $\phi = 0.0160$ /m. Flexural cracks (vertical cracks) occurred at the same spacing as vertical ties, and bond cracks were also observed near the high-strength steel angles at the bottom (see Fig. 9 (a1)). Strength degradation began to occur after the peak point. PB1

Fig. 6. Test setup for flexural test of PSRC girders.

ultimately failed at $\phi_u = 0.0221$ /m ($\mu = 2.98$) due to net section rupture at the bolted joint of bottom angles subjected to tensile loading (refer to Fig. 10).

For PB2 with segmented steel forms used as permanent sheathing (see Fig. 8 (b)), yielding occurred at $\phi_y = 0.0094$ /m and the maximum load (M_u = 3900 kN-m) reached at $\phi = 0.0325$ /m. When compared with PB1, the maximum load was 9.55% greater, whereas the flexural stiffness $EI_{0.75}$ was about 13.7% less due to the increased M_u. A post-yield ductile behavior occurred, and thus the ultimate curvature and ductility were increased to $\phi_u = 0.0336$ /m and $\mu = 3.57$, respectively. As the steel forms reduced concrete cracks, flexural and bond cracks at the bottom subjected to tensile loading were significantly reduced. Instead, as shown in Fig. 9 (b1), one single major crack occurred vertically along the steel form joint at the midspan where flexural rigidity was discontinuous. As with PB1, PB2 ultimately failed by the net section rupture of bottom angles.

For PB3 where five high-strength D32 bars were used for the tensile reinforcement along with the high-strength longitudinal angles (see Fig. 8 (c)), the maximum load and flexural stiffness were greatly increased to M_u = 5420 kN-m and $EI_{0.75}$ = 888,000 kN-m^2, respectively. Yielding occurred at $\phi_y = 0.0061$ /m and the peak point reached at $\phi =$ 0.0091 /m. After the yielding, the strength was maintained almost constant until $\phi_u = 0.0216$ /m ($\mu = 3.54$). As shown in Fig. 9 (c1), flexural cracks in the uniform bending region occurred at the same spacing as the vertical ties. PB3 ultimately failed by the net section rupture of bottom angles subjected to tensile loading. To investigate failure modes further, the cover concrete and transverse ties were removed after testing. As shown in Fig. 10, in the bottom angles subject to tensile loading, hole loosening and subsequent net section rupture occurred at the bolted joint to which the vertical and horizontal ties were connected.

3.2. Strains of longitudinal angles and reinforcing bars

Fig. 11 shows the strains of the longitudinal angles and reinforcing bars used as flexural reinforcements. The horizontal axis denotes the curvature ϕ defined by Eq. (1). The strains were measured at the locations of net and gross sections in midspan between two loading points. Fig. 11 (a) shows the strains BF1, BW1 ~ BW3, TF1 and TW1 ~ TW3 at the location of net section to which vertical and horizontal ties were connected by bolting: the first letter B and T indicate the bottom angles subject to tensile loading and top angles subject to compressive loading, respectively; the second letter F and W indicate the flange and web, respectively. For PB3 in Fig. 11 (a3), the strains of two D32 bars were plotted in the same plane for comparison. Fig. 11 (b) shows the strains BF2, BW4, TF2, and TF4 ~ TF6 at the locations of gross section between adjacent two bolted joints. For clarity, the elastic range of −0.00303 mm/mm ≤ ε ≤ 0.00303 mm/mm was shown as shaded and the yield curvatures ϕ_y were represented with vertical thick lines.

For the bottom angles subject to tensile loading in all specimens, the strains of longitudinal angles were different depending on the locations where they were measured (i.e., the locations of net and gross sections). At the locations of net section (see Fig. 11 (a)), BF1 and BW1 ~ BW3 increased almost linearly until ϕ_y; however, BF1 and BW1 ~ BW3 began to decrease rapidly soon after ϕ_y. Such strain decrease occurred even in the D32 reinforcing bars in PB3 (see Fig. 11 (a3)). On the other hand, at the location of gross section (see Fig. 11 (b)), BF2 and BW4 were remained almost constant at the yield strain or increased further. This indicates that the flexural behavior of the PSRC girders was governed by the net section of longitudinal angles. Thus, the strength and ductility of the PSRC girders were significantly affected by reduction in the cross section of longitudinal angles due to hole drilling. The location where the strains

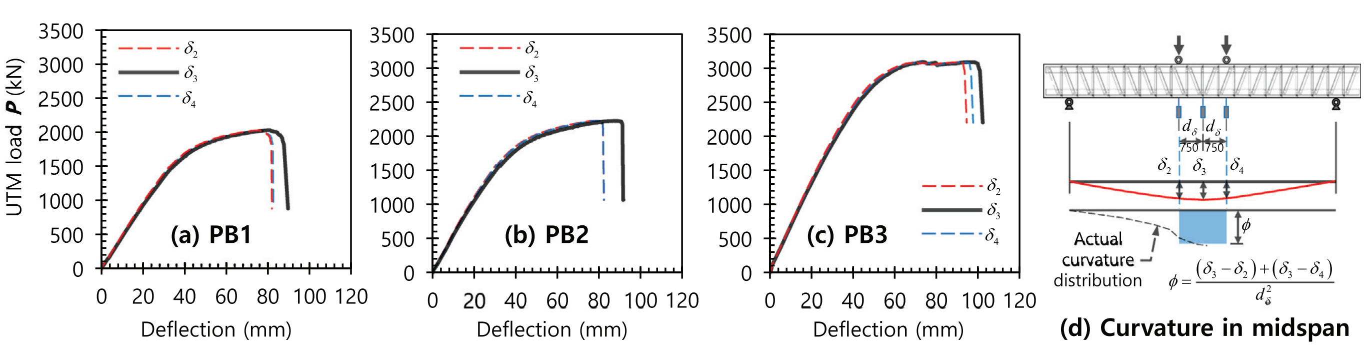

Fig. 7. UTM load-deflection relationships of PSRC girders in midspan.

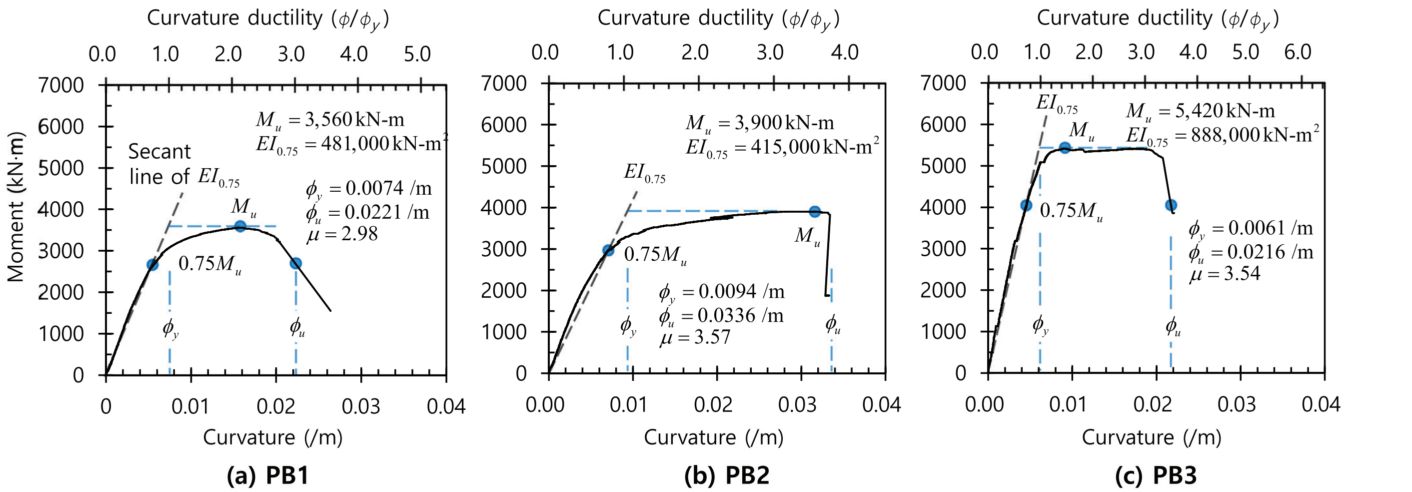

Fig. 8. Moment-curvature relationships of PSRC girders in midspan.

of net section were measured was at the joint where diagonal, vertical, and horizontal ties were connected to one location by fully tensioned high-tension bolts. Since there might be various force transfer mechanisms between the embedded steel members and concrete, such as friction, bearing, and bond, it is difficult to exactly know the force transfer at that location. Nevertheless, the sudden drop in net section strains of bottom angles subject to tensile loading indicates that care should be taken to the reduction in area due to bolt holes and the details of PSRC girders need to be improved further.

For the top angles subject to compressive loading, the strains of longitudinal angles measured at the locations of net and gross sections were almost identical. TF1 and TW1 ~ TW3 at the location of gross section (see Fig. 11(a)), and TF2 and TW4 ~ TW6 at the location of net section (see Fig. 11(b)) all increased almost linearly with increasing ϕ. Note that the compressive strains of the top angles varied with the neutral axis distance. For TF1 and TF2 that were farthest from the neutral axis were the greatest, whereas TW3 and TW6 that were the nearest to the neutral axis were the smallest or even tensile strains.

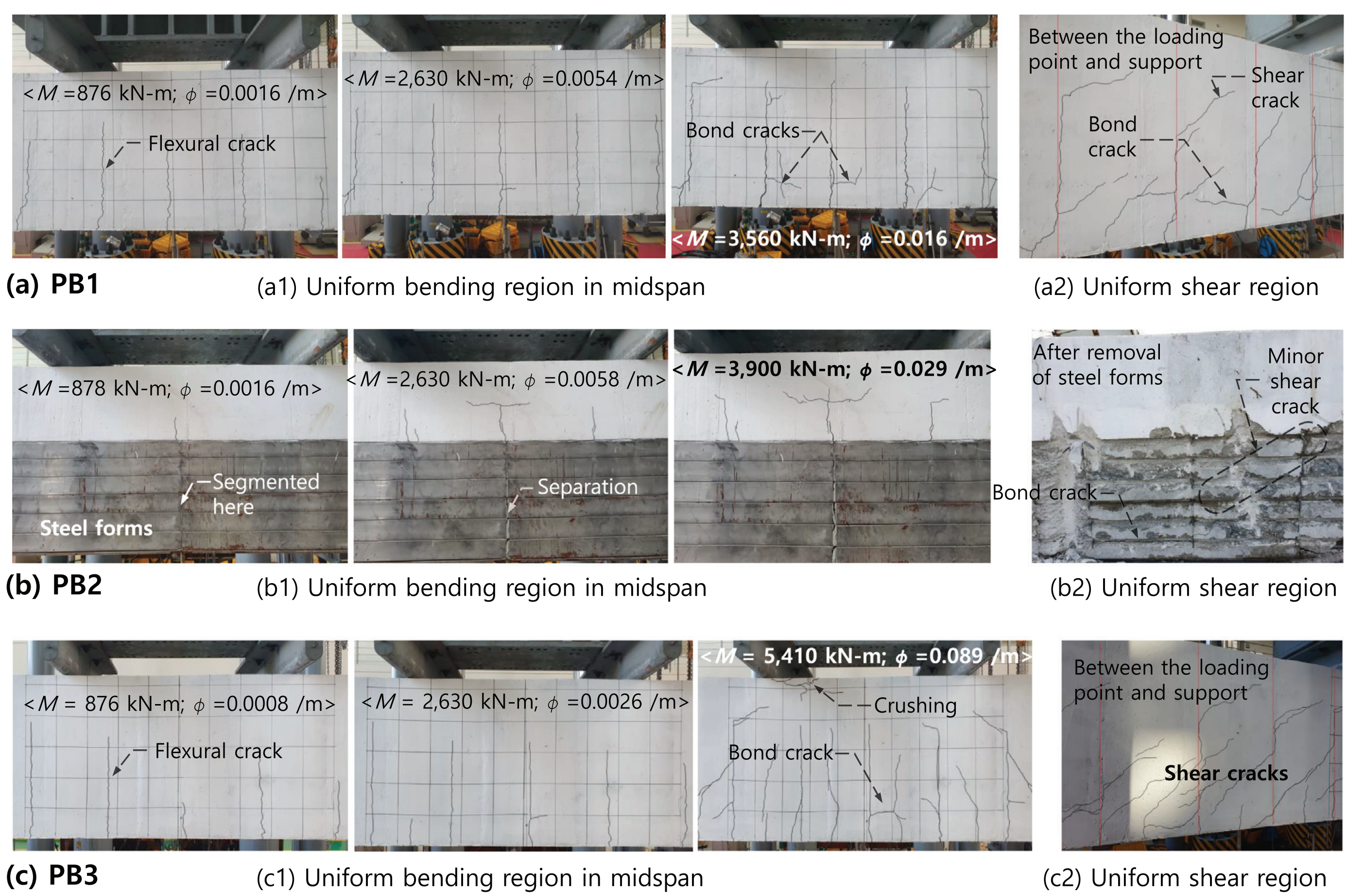

Fig. 9. Concrete cracks in uniform bending and uniform shear regions.

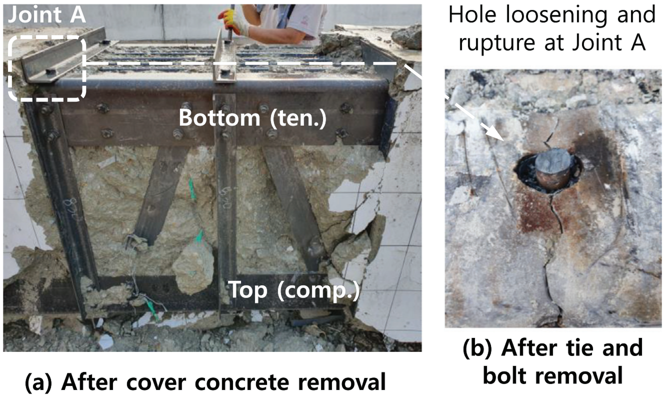

Fig. 10. Net section rupture of longitudinal angles.

3.3. Strains of diagonal and vertical ties

Fig. 12 shows the strains of diagonal (D1 and D2) and vertical (V1 and V2) ties resisting shear in the region of uniform shear. The strains of diagonal and vertical ties measured in PB2 were similar to those of PB1. The horizontal and vertical axes denote the tie strain and moment load, respectively. D1 and V1 were measured by the gauges attached to the legs that were directly connected to the longitudinal angle by bolting, whereas D2 and V2 were measured from the free legs where shear lag was expected to occur. Concrete cracks in the region where V1, V2, D1, and D2 were measured are shown in Figs. 9 (a2), (b2), and (c2). The tie strains in Fig. 12 and concrete cracks in Fig. 9 show the following aspects regarding the shear resistance of PSRC girders.

(1) Diagonal and vertical ties both contributed to the shear resistance. This implies that the shear strengths of the diagonal and vertical ties in PSRC girders can be summed up. Note that D1 and D2 of the diagonal ties were greater than V1 and V2 of the vertical ties. This indicates that the diagonal ties crossing inclined shear cracks resisted shear force more efficiently.
(2) The strains of the legs that were directly connected to the longitudinal angle, D1 and V1, were greater than the strains of the free legs, D2 and V2. This indicates that shear lag occurred at the bolted joint of the diagonal and vertical ties resisting shear.
(3) Shear cracks in PB1 and PB3 in Fig. 9 were the almost same as those occurring in reinforced concrete beams. For PB2 with steel forms (thickness 1.6 mm), shear cracks were significantly reduced or almost vanished. This indicates that the steel sheets were effective in preventing or reducing shear cracks.

4. Flexural and shear strengths

4.1. Plastic stress distribution method and strain compatibility method

The flexural strength of the PSRC girders PB1 ~ PB3 was estimated by the plastic stress distribution method (AISC 360–16) and strain-compatibility method (ACI 318–19). Fig. 13 (a) shows the plastic stresses of steel angles (F_y), reinforcing bars (f_y), and concrete ($0.85f_c'$)

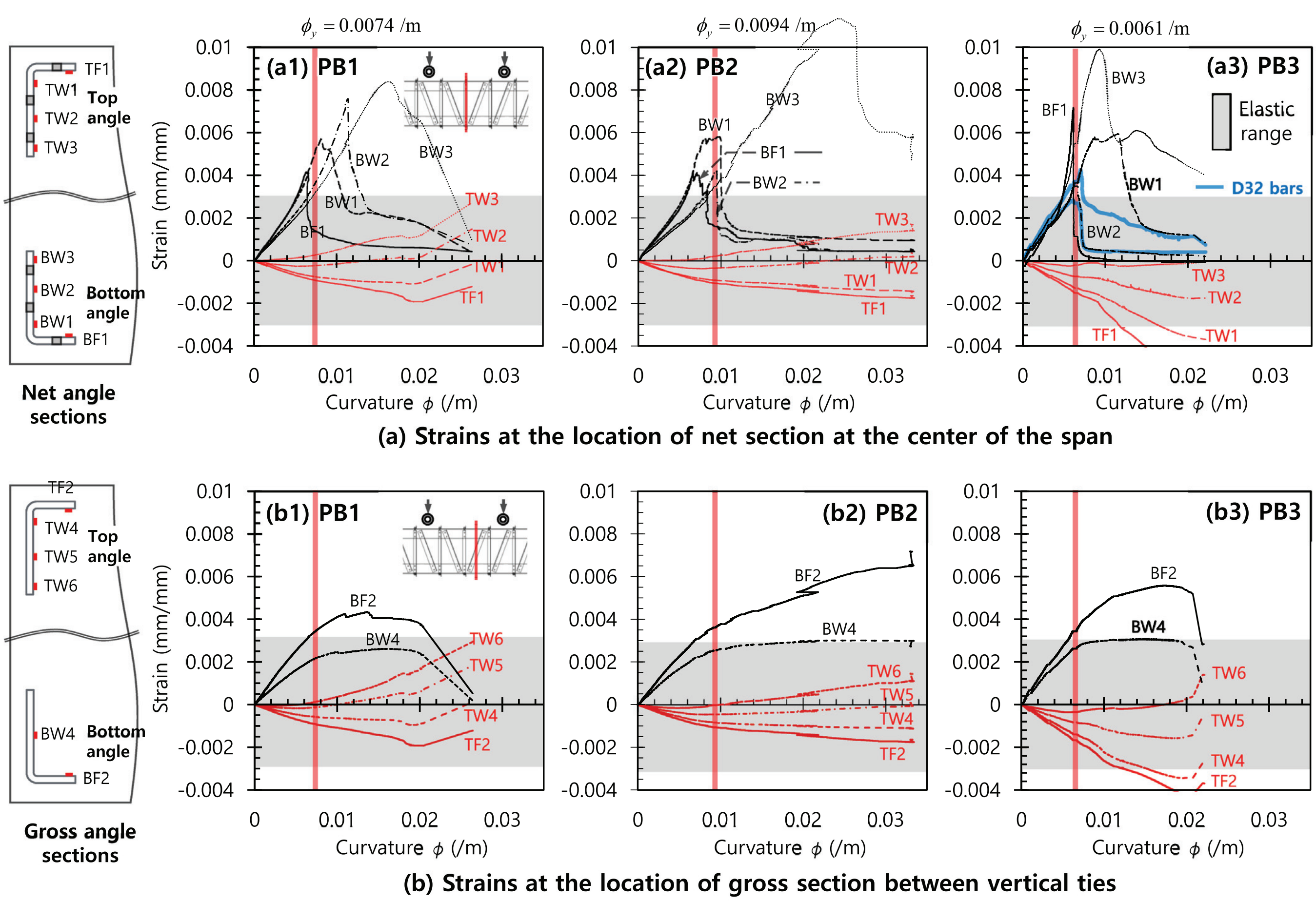

Fig. 11. Strains of longitudinal angles and reinforcing bars varying with curvature.

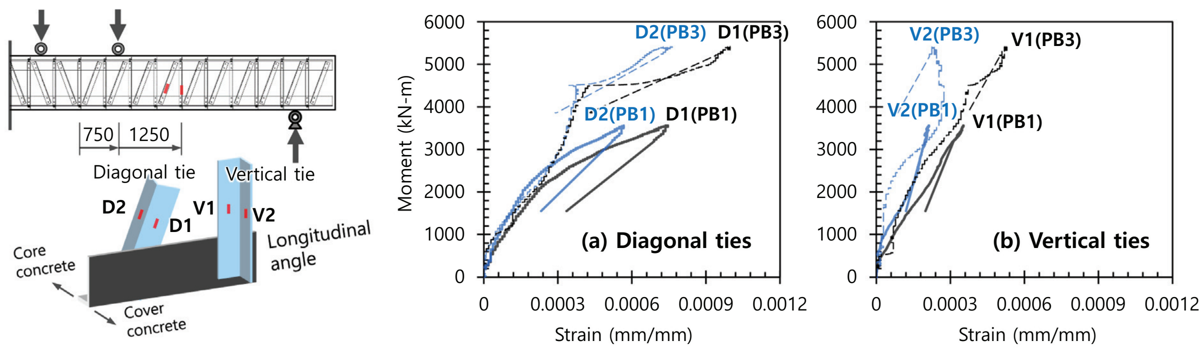

Fig. 12. Strains of diagonal and vertical ties (PB1 and PB3).

across the composite section. Although AISC 360–16 [2] limits the yield strength of structural steel and reinforcing bars not to exceed 525 MPa and 555 MPa, respectively, such strength limits were not considered in the calculations. Fig. 13 (b) shows the strain compatibility method specified in ACI 318–19 [1]. At the ultimate limit state, a linear distribution of strains across the composite section was assumed, with the maximum concrete compressive strain equal to $\varepsilon_{cu} = 0.003$ mm/mm. The stresses of concrete at the compression zone above the neutral axis were approximated as a rectangular stress block of $0.85f_c'$, whereas the stresses of steel angles and reinforcing bars were determined based on the elastic-perfectly plastic stress-strain relationship. High-strength steel angles L-200 × 105 × 15 used in this study were classified as compact sections, and thus effects of local buckling were not considered even after cover spalling.

Since the diagonal and vertical ties were connected by bolting (see Fig. 2), reduction in the cross section of longitudinal angles due to hole drilling was considered in the calculations. Fig. 13 (a) shows the net section of longitudinal angles L-200 × 105 × 15 used as the flexural reinforcement. To connect vertical and horizontal ties, three holes (hole diameter $d_h = 18$ mm) were drilled on the cross section. Thus, the net area of the angle section was $A_{na} = A_a - 3d_h\ t = 3430$ mm^2 ($= 4240 - 3 \cdot 18 \cdot 15$, see Fig. 4 (a)).

Fig. 14 shows the nominal flexural strengths M_{nPSD} and M_{nSCM} by the plastic stress distribution method and strain compatibility method, respectively. M_{nPSD} and M_{nSCM} were calculated using the actual material strengths. Overall, the values of M_{nPSD} and M_{nSCM} (i.e., horizontal straight lines) were in good agreements with the test strengths M_u (i.e., dashed lines): $M_u / M_{nPSD} = 0.98$– 1.13 and $M_u / M_{nSCM} = 0.98$– 1.17. The difference between the nominal flexural strengths by the plastic stress distribution method and strain-compatibility method was almost negligible: $M_{nPSD}/M_{nSCM} = 1.04$ for PB1 and PB2 and 1.00 for PB3.

4.2. Fiber section analysis

The moment-curvature behavior of the PSRC girder specimens was estimated by fiber section analysis based on effective stress-strain relationships of each material. For the fiber section analysis, concrete, steel angles, and reinforcing bars across the PSRC girder section were idealized with finite fiber elements, and then effective stress-strain relationships of each material were applied as follows [4].

For the concrete, a parabolic stress-strain relationship under compressive loading was assumed as follows (see Fig. 15 (a)).

$$\sigma_c(\varepsilon) = \begin{cases} -f_c'\left[2\left|\dfrac{\varepsilon}{\varepsilon_{co}}\right| - \left|\dfrac{\varepsilon}{\varepsilon_{co}}\right|^2\right] & \text{for} -\varepsilon_{cu} \le \varepsilon \le 0 \\ 0 & \text{for } \varepsilon \le -\varepsilon_{cu} \text{ or } \varepsilon \ge 0 \end{cases} \quad (2)$$

where $\sigma_c(\varepsilon)$ = concrete compressive stress for given strain ε; ε_{co} = compressive strain of the concrete corresponding to f_c'; and ε_{cu} = ultimate compressive strain of the concrete. Concrete tensile stress was neglected.

For longitudinal steel angles, a bilinear relationship that simulates the actual material behavior in Fig. 5 was assumed, as follows (see Fig. 16 (b)).

$$\sigma_s(\varepsilon) = \begin{cases} E_s\varepsilon & \text{for } |\varepsilon| \le \varepsilon_y (= F_y/E_s) \\ F_y + E_p(\varepsilon - \varepsilon_y) & \text{for } \varepsilon_y < \varepsilon \le \varepsilon_{r,eff} \\ -F_y + E_p(\varepsilon + \varepsilon_y) & \text{for} -\varepsilon_y > \varepsilon \end{cases} \quad (3)$$

where $\sigma_s(\varepsilon)$ = steel stress for given strain ε; E_s = elastic modulus of the steel; F_y and ε_y = yield stress and strain of the steel; and E_p = post-yield hardening modulus. As shown in Figs. 10 and 11, the deformation capacity of the PSRC girders was limited by net section rupture. Thus, in Eq. (3), the ultimate strain of longitudinal angles under tensile loading

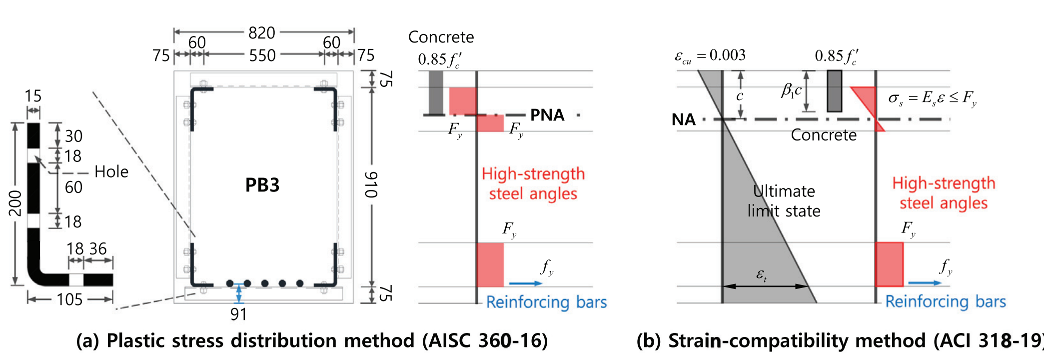

Fig. 13. Flexural strength in PSRC girder section.

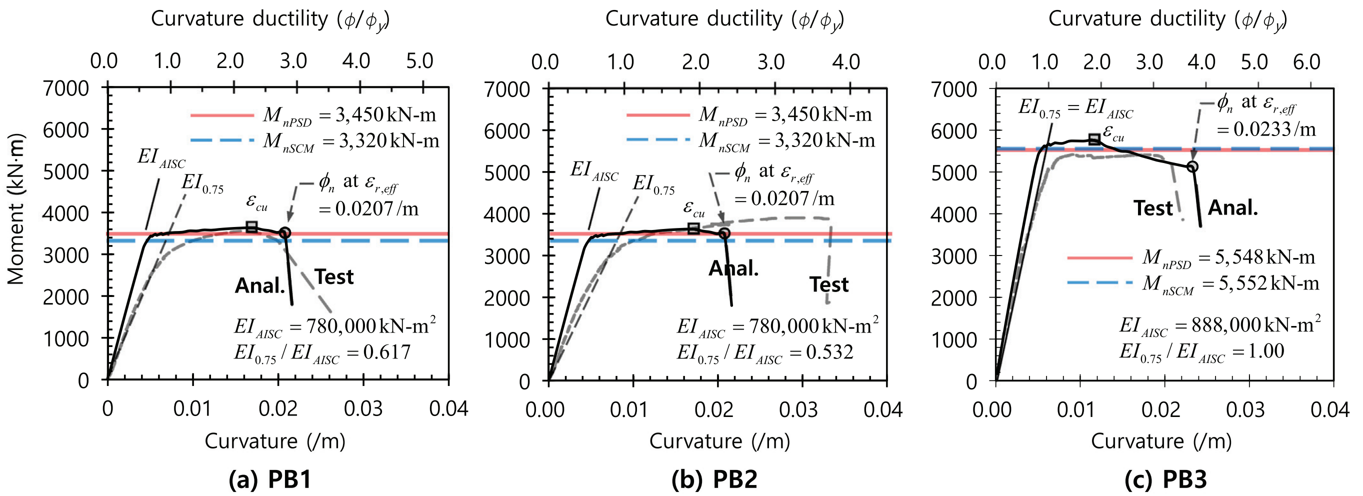

Fig. 14. Comparison between predictions and tests: flexural strength and stiffness, and moment-curvature relationships.

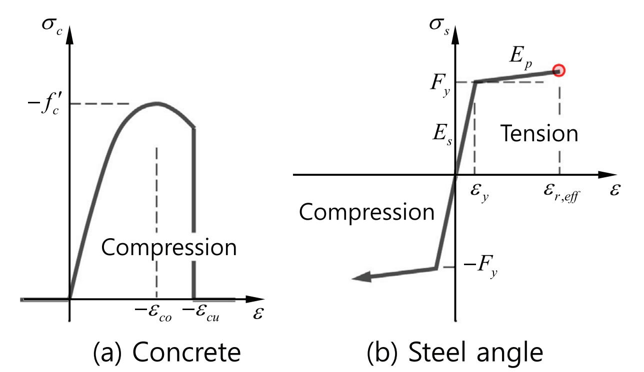

Fig. 15. Effective stress-strain relationships of concrete and high-strength steel angle.

equilibrium condition was satisfied, the moment strength was then computed by adding or subtracting the contributions of all fiber elements. (4) If the extreme fiber strain ε_t of steel angle under tensile loading was equal to or greater than $\varepsilon_{r,eff}$, the analysis was stopped; otherwise, the analysis was repeated by increasing curvature until satisfying $\varepsilon_t = \varepsilon_{r,eff}$.

Material properties used for the fiber section analysis were as follows: for the concrete, $f_c' = 36.3$ MPa, $\varepsilon_{co} = 0.002$ mm/mm, and $\varepsilon_{cu} = 0.003$ mm/mm; for longitudinal angles, $F_y = 605$ MPa, $E_s = 200$ GPa, $E_p = 1070$ MPa, and $\varepsilon_{r,eff} = 0.003 + 18 \cdot 0.398/500 = 0.0174$ mm/mm; for D32 reinforcing bars, $f_y = 662$ MPa, $E_s = 200$ GPa, and $E_p = 1,540$ MPa.

Fig. 14 compares the moment-curvature (M-ϕ) relationships by the fiber section analysis and tests. Black solid lines represented the analysis, while gray dashed lines represented the test. For the analysis, the was limited not to exceed the effective rupture strain $\varepsilon_{r,eff}$. The effective rupture strain $\varepsilon_{r,eff}$ of longitudinal angles was defined as follows.

$$\varepsilon_{r,eff} = \frac{\varepsilon_y(s - d_h) + \varepsilon_r d_h}{s} \approx \varepsilon_y + \frac{d_h \varepsilon_r}{s} \tag{4}$$

where ε_r = maximum elongation strain at rupture; d_h = diameter of bolt holes at the angle section; and s = spacing of transverse ties. $\varepsilon_{r,eff}$ was suggested from the test observations that angle elongations under tensile loading was mainly concentrated in the narrow region of net section. In Eq. (4), $d_h\varepsilon_r$ is the tensile deformation at rupture in the narrow region of net section, while $\varepsilon_y[s\text{-}d_h]$ is the deformation in the remaining region of gross section. Thus, $\varepsilon_{r,eff}$ represents the average tensile strain of the longitudinal angle in between adjacent two ties (spacing s).

For reinforcing bars, the same bilinear relationships as those in Eq. (3) were used to simulate the strain-hardening behavior in Fig. 5, with the following modifications. First, material properties including yield strength and elastic modulus were replaced by those for reinforcing bars. Second, $\varepsilon_{r,eff}$ was not applied.

The fiber section analysis was performed by increasing curvature ϕ from 0 to an ultimate value, as follows. (1) For a given curvature ϕ, the strains of fiber elements of each material were determined by assuming the depth of the neutral axis, and the stresses of the concrete, steel angle, and reinforcing bar elements were then calculated from stress-strain relationships of each material. (2) By summing the internal tensile and compressive forces of all fiber elements, the equilibrium condition across the composite section was checked. (3) If the

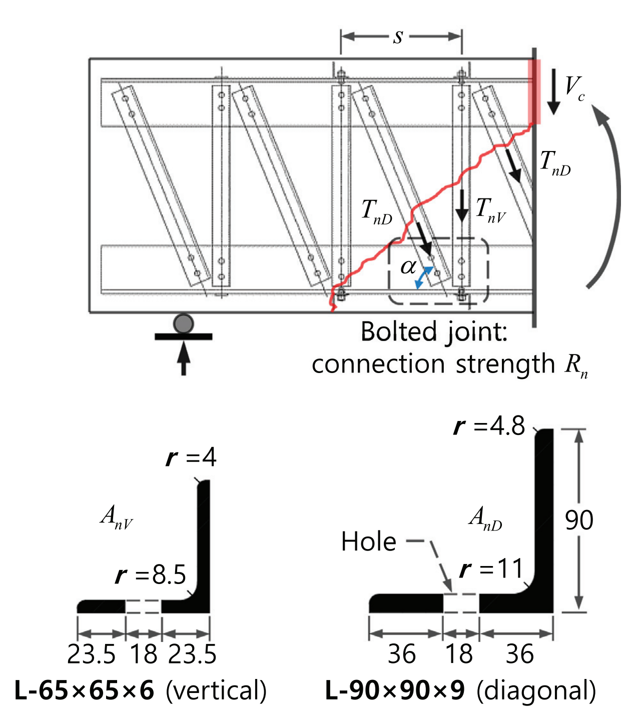

Fig. 16. Shear strength of PSRC girders.

points of maximum strength (M_n) at which the extreme fiber strain of concrete reached $\varepsilon_{cu} = 0.003$ mm/mm were marked as gray squares, whereas the points of maximum curvature ϕ_n at which the extreme tensile strain of longitudinal angles reached $\varepsilon_{r,eff}$ ($= 0.0174$ mm/mm) were marked as gray circles. Overall, the M- ϕ behavior by the analysis agreed with the test with reasonable precision. In all specimens, the strengths showed good agreements between the analysis and test ($M_u/M_n =$ 0.94– 1.07). On the other hand, the flexural stiffness representing the elastic behavior before yielding was considerably overestimated by the analysis. This indicates that there might be bond slip on the smooth surface of longitudinal angles, which can be inferred from the fact that the difference between the measured and predicted stiffnesses was significantly reduced in PB3 with deformed bars.

The maximum curvatures ϕ_n of PB1 and PB3 at which the extreme fiber strain of longitudinal angles reached $\varepsilon_{r,eff}$ were in good agreements with the test results: $\phi_u/\phi_n = 1.07$ for PB1 and 0.93 for PB3. On the other hand, for PB2 with steel forms, the ϕ_u/ϕ_n ratio was increased to 1.62. Note that $\varepsilon_{r,eff}$ is valid only when the predominant failure mode is the net section rupture of longitudinal angles. For example, for the longitudinal angles considered in this study, the yield strength corresponding to gross section yield, $F_yA_a = 2850$ kN, was larger than the fracture strength corresponding to net section rupture, $F_uA_{na} = 2080$ kN, and consequently the governing limit state was the net section rupture. However, such net section rupture may not be favorable for securing seismic performance. Thus, care should be taken when the PSRC girder is used in high-seismic zones.

4.3. Flexural stiffness

Since most design codes adopt the limit state design method based on the ultimate capacity, the elastic analysis to determine required strength needs to be based on effective stiffness, rather than initial stiffness. Thus, the measured flexural stiffness $EI_{0.75}$, defined as the slope of secant lines connecting the origin and the pre-peak point of $0.75M_u$ was compared with the nominal flexural stiffness EI_{AISC} specified in AISC 360–16 (see Fig. 8). According to AISC 360–16 Sec. I1 and I2, EI_{AISC} of encased composite members can be calculated as follows.

$$EI = 0.64EI_{eff} = 0.64(E_sI_s + 0.5E_sI_{sr} + C_1E_cI_c) \tag{5}$$

where I_s, I_{sr}, and I_c = moments of inertia of the steel angles, reinforcing bars, and uncracked concrete section about the elastic neutral axis of the PSRC girder section, respectively; E_c = elastic modulus of the concrete ($= 0.043w_c^{1.5}\sqrt{f_c'}$); w_c = weight of the concrete per unit volume ($= 2400$ kg/m^3); $C_1 = [0.25 + 3(A_s + A_{sr})/A_g] \le 0.7$; and A_s, A_{sr}, and A_c = areas of the steel angles, reinforcing bars, and concrete section, respectively.

Fig. 14 and Table 2 show the EI_{AISC} values of the PSRC girder specimens calculated by Eq. (5). For comparison, the measured values $EI_{0.75}$ were also shown in the same figure and table. All stiffness values in Table 2 were presented as the ratios to the elastic stiffness of the uncracked concrete section, E_cI_g. For PB1 and PB2, the EI_{AISC} values were greater than the $EI_{0.75}$ values ($EI_{0.75}/EI = 0.617$ and 0.532). Instead, EI_{AISC} better fitted to the M-ϕ curve by the fiber section analysis. On the other hand, for PB3 with additional reinforcing bars, the EI_{AISC} value was the same as the measured one (i.e., $EI_{0.75}$), while the M-ϕ curve by the fiber section analysis slightly overestimated the stiffness (see the thick solid line in Fig. 8 (c)).

As with reinforced concrete beam sections, the PSRC girders used longitudinal steel angles as flexural reinforcement inside the concrete section. Thus, the flexural stiffness of the PSRC girders were compared with the nominal flexural stiffness EI of reinforced concrete beams in ACI 318–19 (design code for new concrete buildings) and ASCE 41–17 [3] (guideline for seismic evaluation of existing buildings). ACI 318–19 uses $EI = 0.35E_cI_g$ for elastic analysis at factored load level, while ASCE 41–17 uses $EI = 0.3E_cI_g$ for linear procedures. Table 2 compares the EI values in accordance with ACI 318–19 and ASCE 41–17 with the measured ones (i.e., $EI_{0.75}$). Overall, the EI values of ACI 318–19 and ASCE 41–17 were comparable to EI_{AISC} by Eq. (5). For PB1 and PB2 where the tensile reinforcement ratio was relatively less ($\rho = 0.5A_s/bd =$ 0.0113), the EI values of ACI 318–19 and ASCE 41–17 were greater than $EI_{0.75}$. On the other hand, for PB3 with the greater tensile reinforcement ratio ($\rho = [0.5A_s + A_{sr})/bd] = 0.0164$), the EI values of ACI 318–19 and ASCE 41–17 were comparable to $EI_{0.75}$.

When conducting elastic analysis to determine member forces and deformations, the flexural stiffness of the existing design and evaluation codes is assigned to the entire beam or girder length spanning between columns. Unlike this, $EI_{0.75}$ on the M-ϕ curves in Fig. 14 is the flexural rigidity at a section (i.e., at the critical section in midspan). Thus, the nominal flexural stiffness in Table 2 that was greater than $EI_{0.75}$ may be reasonable.

4.4. Shear strength

Basically, the shear strength of PSRC girder is provided by the concrete and transverse ties (i.e., diagonal and vertical ties). According to ACI 318–19 and AISC 360–16, the nominal shear strength V_n of PSRC girder can be estimated as follows (see Fig. 16).

$$V_n = \frac{1}{6}\sqrt{f_c'}bd + 2T_{nV}\frac{d}{s} + 2T_{nD}(\sin\alpha + \cos\alpha)\frac{d}{s} \tag{6}$$

$$T_{nV} = F_{yV}A_{nV}U \le R_n \tag{7}$$

$$T_{nD} = F_{yD}A_{nD}U \le R_n \tag{8}$$

where b = width of the concrete section; d = effective depth of the composite section, defined as the distance from the geometric center of the tensile angle to the outmost end of the concrete compression zone; F_{yV} and F_{yD} = steel yield strengths of the vertical and diagonal ties, respectively; A_{nV} and A_{nD} = net section areas of the vertical and diagonal ties, respectively; U = coefficient that accounts for shear lag in the bolted joint of angle section (= 0.6, AISC 360–16); s = spacing of the vertical and diagonal ties; and α ($\ge 30°$) = inclination angle of the diagonal ties relative to the longitudinal axis of the girder. In Eq. (6), the number 2 is multiplied as the vertical and diagonal ties are placed on

Table 2
Nominal flexural stiffness values.

Spec.	Test values[1] $EI_{0.75}/[E_cI_g]$	Nominal flexural stiffness[1]			
		AISC 360–16 $EI_{AISC}/[E_cI_g]$ ($EI_{0.75}/EI_{AISC}$)	ACI 318–19 (Table 6.6.3.1.1(a)) $EI/[E_cI_g]$	ACI 318–19 Alternative[2] (Table 6.6.3.1.1(b)) $EI/[E_cI_g]$	ASCE 41–17 $EI/[E_cI_g]$
PB1	0.208	0.337 (0.617)	0.35	0.391	0.30
PB2	0.179	0.337 (0.532)	0.35	0.391	0.30
PB3	0.383	0.383 (1.000)	0.35	0.521	0.30

[1] All stiffness values are the ratios to E_cI_g, where $E_c = 28.5$ GPa and $I_g = 0.0814$ m^4.
[2] $EI = (0.1 + 25\rho)(1.2–0.2b/d)E_cI_g$ where $\rho = 0.0113$ for PB1 and PB2 and 0.0164 for PB3, $b = 820$ mm, and $d = 913$ mm for PB1 and PB2 and 931 mm for PB3.

Table 3
Shear strengths.

Specimen	Concrete (kN)	Vertical ties (kN)		Diagonal ties (kN)		Shear strength V_n (kN)	Shear load V_u (kN)
		Tensile strength T_{nV}	Joint strength R_n	Tensile strength T_{nD}	Joint strength R_n		
PB1 ~ PB3	755[1]	135[2]	106[3]	280[4]	106[3]	1640[5]	1020– 1550[6]

[1] $d \fallingdotseq 913$ mm for all specimens
[2] $A_{nV} = 636$ mm^2.
[3] The joint strength was determined as the slip strength of the interface: $R_n = n_b(\mu T_o) = 2 \cdot 0.5 \cdot 106 = 106$ kN
[4] $A_{nD} = 1380$ mm^2.
[5] Eq. (6) for $b = 820$, $d = 913$ mm, $s = 500$ mm, $\alpha = 67.7°$, and $T_{nV} = T_{nD} = R_n = 106$ kN.
[6] 1020 kN for PB1, 1110 kN for PB2, and 1550 kN for PB3.

both sides of the girder. For the vertical and diagonal ties, steel angles are bolted only on one leg (see Fig. 16). Thus, the shear lag coefficient $U = 0.6$ is multiplied in Eqs. (7) and (8).

The tensile strengths T_{nV} and T_{nD} of the vertical and diagonal ties, respectively, cannot be larger than the connection strength R_n at the bolted joint. According to AISC 360–16, the connection strengths corresponding to the design limit states such as bolt shear rupture, angle block shear rupture, bolt hole bearing, and interface sliding can be computed as follows.

$$R_n = \min \begin{cases} n_b(F_{nvb}A_b) \text{ for bolt shear rupture} \\ 0.6F_uA_{nv} + F_uA_{nt} \le 0.6F_yA_{gv} + F_uA_{nt} \text{ for block shear rupture} \\ 1.2L_ct_aF_u \le n_b(2.4d_bt_aF_u) \text{ for bolt hole bearing} \\ n_b(\mu T_o) \text{ for interface sliding} \end{cases} \quad (9)$$

where n_b = number of bolts used at the joint; F_{nvb} = shear strength of high-tension bolt, taken as $0.45F_{ub}$; F_{ub} = ultimate strength of high-tension bolt; F_y and F_u = steel yield strength and steel ultimate strength of the vertical or diagonal angle; A_{nv}, A_{gv}, and A_{nt} = net section area for shear, gross section area for shear, and net section area for tension along the perimeter of block shear rupture; L_c = net spacing of bolts in the direction of loading; t_a = angle thickness; d_b = bolt diameter; μ = frictional coefficient at the faying surface (= 0.5 for not-painted, sand-blasted surface); and T_o = design pretension of one single fully-tightened high-tension bolt.

Table 3 shows the shear strength of the PSRC girder specimens. The tensile strengths of the vertical and diagonal ties were determined as the slip strength at the bolted joint, contributed by two F10T M16 bolts: $T_{nV} = T_{nD} = R_n = 106$ kN. Thus, the nominal shear strength of PB1 ~ PB3 computed by Eq. (6) was $V_n = 1640$ kN. Although the shear load $V_u = 1550$ kN of PB3 was close to the nominal shear strength V_n, concrete cracks in Fig. 9 (c2) and strains of longitudinal angles in Fig. 12 were not significant. This indicates that the nominal shear strength by Eq. (6) might be conservative. For the shear capacity of PSRC girders, further study is required.

5. Discussion of design application

Based on the results discussed previously, design considerations of PSRC girders with longitudinal angles and bolt-connected transverse ties were given as follows.

1. The flexural strength of PSRC girders can be determined by the plastic stress distribution method and strain-compatibility method, specified in AISC 360–16 and ACI 318–19. In addition, fiber section analysis based on a linear distribution of strains across the composite section and effective stress-strain relationships of each material can be used. For the fiber section analysis, perfect bond between the steel angles and concrete can be assumed. Reduction in the cross-sectional area due to hole drilling should be considered for longitudinal angles under tensile and compressive loadings both, and the ultimate strain of the angles under tensile loading should be limited to $\varepsilon_{r,eff}$ defined in Eq. (4).
2. The nominal flexural stiffness specified in AISC 360–16 ($0.64EI_{eff}$, see Eq. (5)) can be used for elastic analysis at factored load level to determine member forces for strength design.
3. The shear strength can be calculated by summing the contributions of concrete and transverse ties (i.e., vertical and diagonal ties) in accordance with Eqs. (6) (8). The tensile strength of the transverse ties, T_{nV} and T_{nD}, should be not greater than the connection strength R_n at the bolted joint (see Eq. (9)).

In this study, the number of specimens were only three and design variables considered were limited. Thus, to apply PSRC girders to design practice, further study is required.

6. Summary and conclusions

This study investigated the behavior of PSRC girders with longitudinal angles and bolt-connected transverse ties. The findings of this study are summarized as follows.

1. Reduction in the cross-sectional area of longitudinal angles due to hole drilling significantly affected the load-deformation behavior and failure mode of the PSRC girders. The governing limit state was net section rupture.
2. The nominal flexural strengths by the plastic stress distribution method and strain-compatibility method in accordance with current design codes, such as AISC 360–16 and ACI 318–19, agreed well with the test strengths. The nominal shear strength determined by summing the contributions of the concrete and transverse steel ties in accordance with ACI 318–19 were conservative. The nominal flexural stiffness specified in AISC 360–16 and ACI 318–19 was comparable to or greater than the test.
3. Fiber section analysis based on effective stress-strain relationships of each material predicted the moment-curvature behavior of the PSRC composite sections with reasonable precision. The analysis strengths agreed well with the test values. In particular, the maximum curvature controlled by net section rupture was captured using the effective rupture strain $\varepsilon_{r,eff}$ of longitudinal angles.

Data availability

All data, models, and code generated or used during the study appear in the submitted article.

Declaration of Competing Interest

The authors declare that they have no known competing financial interests or personal relationships that could have appeared to influence the work reported in this paper.

Acknowledgement

This work was supported by the Korea Agency for Infrastructure Technology Advancement (20CTAP-C157615) funded by the Ministry of Land, Infrastructure, and Transport of Korea.

References

[1] ACI Committee 318, *Building Code Requirements for Structural Concrete*, ACI 318–19, American Concrete Institute, Farmington Hills, MI, 2019.
[2] American Institute of Steel Construction, *Specification for Structural Steel Building*, AISC 360–16, Chicago, Illinois, 2016.
[3] American Society of Civil Engineers / Structural Engineering Institute, *Seismic Evaluation and Retrofit of Existing Buildings*, ASCE/SEI 41–17, American Society of Civil Engineers, Reston, Virginia, 2017 (623p).
[4] T.S. Eom, H.J. Hwang, H.G. Park, C.N. Lee, H.S. Kim, Flexural test for steel-concrete composite members using prefabricated steel angles, J. Struct. Eng. 140 (4) (2014), 04013094.
[5] T.S. Eom, J.Y. Yang, D.Y. Kim, J.J. Lim, S.H. Lee, Experimental investigation of bolted end-plate angle splice in encased composite columns, Eng. Struct. 190 (2019) 31–40.
[6] T.S. Eom, J.J. Lim, J.W. Kim, Axial compressive behavior of concrete-encased high-strength steel angle columns, J. Struct. Eng. 147 (4) (2021) https://doi.org/10.1061/(ASCE)ST.1943-541X.0002908.
[7] H.J. Hwang, T.S. Eom, H.G. Park, S.H. Lee, Axial load and cyclic load tests for composite columns with steel angles, J. Struct. Eng. 142 (5) (2016), 04016001.
[8] H.J. Hwang, T.S. Eom, H.G. Park, S.H. Lee, H.S. Kim, Cyclic loading test for beam-column connections of concrete-filled U-shaped steel beams and concrete-encased steel angle columns, J. Struct. Eng. 141 (11) (2015), 04015020.
[9] C.S. Kim, H.J. Hwang, Numerical investigation on load-carrying capacity of high-strength concrete-encased steel angle columns, International Journal of Concrete Structures and Materials 12 (2018) 11, https://doi.org/10.1186/s40069-018-0238-7.
[10] C.S. Kim, H.G. Park, K.S. Chung, I.R. Choi, Eccentric axial load capacity of high-strength steel-concrete composite columns of various sectional shapes, J. Struct. Eng. 140 (4) (2014).
[11] C.S. Kim, H.G. Park, H.J. Lee, I.R. Choi, K.S. Chung, Eccentric axial load test for high-strength composite columns of various sectional configurations, J. Struct. Eng. 143 (8) (2017), 04017075.
[12] H.J. Kim, H.J. Hwang, H.G. Park, D.K. Kim, Concentric axial load test for composite columns using bolt-connected steel angles, Eng. Struct. 214 (2020) 110650.
[13] H.J. Kim, H.J. Hwang, H.G. Park, Eccentric-axial-load test for composite columns using bolt-connected steel angles, J. Struct. Eng. 146 (9) (2020), 04020178.